J Therm Spray Tech
https://doi.org/10.1007/s11666-024-01805-4

ORIGINAL RESEARCH ARTICLE

Martensite Formation and Dynamic Recrystallization in Cold Sprayed SS304L

Christopher M. Roper[1] · C. Jacob Williamson[1] · Ke An[2] · Luke N. Brewer[1]

Submitted: 23 March 2024 / in revised form: 30 May 2024 / Accepted: 26 June 2024

Abstract In this study, a comprehensive set of characterization techniques are employed to demonstrate that the cold spray deposition process can result in a significant increase in martensite in austenitic stainless steel. The lack of consensus in the literature on the formation of strain-induced martensite in cold spray can be attributed to the diverse processing conditions and measurement techniques used in different studies. In this work, EBSD, neutron diffraction, TEM imaging, and precession electron diffraction were used in combination to examine whether strain-induced martensite is formed during cold spray deposition of 304L stainless steel powder and to give further insight into possible mechanisms controlling this phenomenon. Cold spray was performed at both 350 °C and room temperature (25 °C) to investigate the effects of spray temperature on the martensite transformation. It is shown that the strain-induced martensite formation is significantly suppressed compared to that which would be expected for comparable levels of plastic strain at quasi-static strain rates. Additionally, the spray gas temperature is shown to directly impact the microstructure formed at the prior particle interface and the formation of dynamically recrystallized regions.

Keywords austenite-to-martensite phase transformation · cold spray · EBSD · neutron diffraction · STEM

✉ Christopher M. Roper
cmroper@crimson.ua.edu

[1] Department of Metallurgical and Materials Engineering, The University of Alabama, 3047 HM Comer, Tuscaloosa, Al 35487-0202, USA

[2] Chemical and Engineering Materials, Oak Ridge National Laboratory, Oak Ridge, TN 37831, USA

Introduction

Cold gas dynamic spray, or cold spray (CS), is a solid-state additive manufacturing technique that uses high-pressure gas to accelerate particles (typically 15-45 μm in diameter) to a high velocity (typically 300-2500 m/s) through a de Laval converging-diverging nozzle (Ref 1). This rapid velocity results in plastic deformation of the particles upon impact, resulting in bonding and a dense deposition with minimal porosity. After cold spray deposition, spherical particles experience an average plastic strain of 50-90% (Ref 2). As this plastic strain is experienced by small particles moving at high velocities, the average strains or strain rates during particle impact are not uniform over the impacting particle. Literature reports strain rates in the prior particle interiors of 10^4 to 10^5 s^{-1} (Ref 3) and 10^7 s^{-1} to 10^9 s^{-1} in the adiabatic shear zones at the prior particle interface (Ref 3-5).

Due to both the extent of plastic strain during cold spray and the tendency of austenitic stainless steels to form strain-induced martensite under deformation, the question of whether CS promotes deformation-induced martensite in austenitic stainless steel has arisen in cold spray literature. The strain-induced martensite transformation in austenitic stainless steels is a well-known phenomenon that is comprehensively reported in literature (Ref 6-11). The literature on cold spray of austenitic stainless steels consists of two categories, one consisting of those that report a secondary BCC phase in the deposit which is attributed to the initial powder feedstock microstructure (Ref 12-14), and a second category consisting of those that show no formation of martensite in depositions produced using single-phase initial feedstock powder (Ref 15-18). Notably, work by Borchers et al. showed a reduction in martensite measured

Published online: 08 July 2024

by x-ray diffraction XRD relative to the powder feedstock after cold spray deposition in SS316 (Ref 19).

Strain-induced martensite can significantly affect both the mechanical properties and the corrosion behavior of austenitic stainless steels, and for this reason, it has been widely studied since the introduction of these alloys in the early twentieth century. The formation of metastable strain-induced martensite in austenitic stainless steels such as SS304(L) and SS316(L) was first reported in 1932 by Erich Scheil (Ref 20). Later work by T. Angel in 1954 greatly expanded upon the understanding of this transformation (Ref 21). Work by Venables (Ref 22) and later by Lagneborgj (Ref 23) showed that ε, an hcp phase, can serve as a precursor to strain-induced martensite (α') to initiate strain induced martensite embryos in austenitic stainless steels. Further work by P. Mangonon et al. in 1970 showed that strain-induced martensite is formed by the sequence of $\gamma \rightarrow \varepsilon \rightarrow \alpha'$, where γ is the austenite phase, ε is an hcp phase, and α' is the strain-induced body centered tetragonal (BCT) phase (Ref 24). Additionally, this work by Mangonon et al. shows that the nucleation of α' can occur heterogeneously at intersections of ε bands or where ε bands abut twin or grain boundaries. Both Lagneborgj and Goodchild et al. later show that while the ε phase is often formed at these shear band intersections, it is not necessary for the formation of α' and that, while less common, α' can be generated in grains that are oriented in $< 001 >$ orientation relative to the compression axis (Ref 25).

The strain-induced martensite transformation, as it applies to high strain rate transformations, has been more thoroughly researched outside of the context of cold spray deposition. A series of works by Olson et al. proposes that at low strain levels, α' forms more readily during high strain rate tension than low-rate tension, in an idea known as the Olson-Cohen analysis (Ref 26-30). However, studies of stress amplitude and strain rate on the martensitic phase transformation performed by Murr et al., Hecker et al., and Staudhammer et al. demonstrated that at larger total strains (above 0.25), adiabatic heating due to straining begins to play a significant role in reducing the driving force for the $\gamma \rightarrow \alpha'$ transformation (Ref 31-34). Furthermore, Murr et al. proposed that α' only occurs at shear band intersections where the definition of shear bands consists of bundles of faults, twins, and the ε phase. They postulated that the "growth" of the α' phase is not growth but the coalescence of the α' embryos. At high strain rates, this coalescence is also inhibited, further restricting the α' product.

The objective of this current study is to investigate the presence of martensite in cold sprayed SS304L deposits and to evaluate whether additional strain-induced martensite is formed during the cold spray process due to the plastic deformation upon initial impact as well as from the subsequent peening by other impinging particles. Cold spray provides a unique set of conditions, such as high strain rates, elevated temperatures, repeated particle peening, and small grain sizes, which are not easily replicated in other metal forming processes. Due to this unique set of circumstances, investigating the strain-induced martensite transformation in cold sprayed austenitic stainless steel is worthwhile. The mechanisms that promote or inhibit the strain-induced martensite phase transformation in cold sprayed material are investigated using a combination of neutron diffraction, electron backscatter diffraction (EBSD), transmission electron microscopy (TEM), and precession electron diffraction (PED).

Methods

In this study, SS304L was deposited via cold spray onto a 3.18-mm (1/8") thick SS304L substrate using a VRC GEN III high pressure cold spray system (VRC Metal Systems, Rapid City, SD). Inert gas atomized powder was acquired from Sandvik Osprey Ltd. with a nominal particle size of 15-45 μm was used (see composition in Table 1). Sieve analysis showed the particle size to be 99.8% $-$ 45 + 15 μm with 0.2% being + 45 μm, while laser diffraction analysis showed the d10, d50, and d90 to be 28.7 μm, 40.5 μm, and 55.5 μm, respectively. A de Laval converging-diverging nozzle was used with a throat size of 2.00 mm and a length of 196 mm. Helium gas was used as the spray gas with a pressure of 600 psi (4.14 MPa) and spray gas temperatures of 350 °C and 25 °C, respectively, for the two conditions investigated. The temperature measurement of the spray gas is collected in the spray system using a thermocouple just prior to the process gas entering the converging section of the nozzle; therefore, these temperatures can also be correlated to the stagnation temperatures for the runs. Four layers were deposited, each with a layer thickness of 0.5 mm for a nominal deposit thickness of 2 mm for each sample and an overall size for the depositions of 25 × 25 × 2 mm. The gun velocity during deposition was 100 mm/s.

The cold spray specimen was prepared for neutron diffraction measurements by using electrical discharge machining (EDM) to section a square from the center of the deposition 20 × 25 mm in size. Two powders were also

Table 1 Measured chemical composition of the 304L stainless steel powder (wt. %)

C	N	Mn	P	S	Si	Cr	Ni	Fe
0.02	0.14	1.5	0.023	0.006	0.73	18.7	8.3	Balance

prepared for neutron diffraction, one was an as-received powder, and another was heat treated at 750 °C for 1 h in a furnace to ensure complete recrystallization. A vanadium canister was used for measurements of the metal powders. A gauge volume of 0.3 × 17 × 6 mm and a 30-Hz chopper were used, resulting in a wavelength of 2.88 Å with a collection time of 15 minutes per data point. Each of the powder samples used a 5-mm beam with a collection time of 5 min. Phase fraction from the neutron diffraction results was calculated using the VDRIVEX and GSAS software to perform Rietveld refinement. Neutron diffraction was chosen over laboratory- based XRD due to more accurate quantification and better detection of minor phase fractions. EBSD was performed on a JOEL 700 FE SEM using an accelerating voltage of 20 kV and a step size of 0.125 μm from the same material used to make the samples for neutron diffraction. Samples for TEM and PED were made using a Tescan FIB from the same material used for EBSD.

While EBSD gives us an excellent look at the cold spray microstructure and the overall phase distribution in the material, the reliability of pattern indexing at the prior particle interfaces is lacking due to the high amount of deformation at the prior particle interfaces and the small grain size. For this purpose, TEM imaging and precession electron diffraction (PED) were performed to gain a higher resolution image at these areas and investigate both the grain structure as well as the phase fraction distribution at the prior particle interfaces. The prior particle interface was lightly etched with Kalling's No. 2 etchant prior to FIB lift out to identify the prior particle interfaces. An FEI Tecnai F-20 operating at 200 keV was used for TEM imaging, and PED was performed using the Topspin software on the Nanomegas ASTAR system. The PED scans were done using a 30-micron condenser aperture with a 3-nm step size, a precession angle of 0.5 degrees, with ten precessions per frame. Grain orientation spread (GOS) maps were used to look for the possibility of dynamically recrystallized grains. GOS maps assign a single color to each grain based on the total average spread from the median orientation angle for all points in a grain. This means that recrystallized grains with a low defect density, and therefore, a lower spread will have a smaller value, while highly deformed grains with a large defect density will have a much larger value.

Results

EBSD mapping of the as-received powder (Fig. 1) and the cold sprayed austenitic stainless steel (Fig. 2) shows the presence of a second phase. This phase is either the ferrite BCC phase or the martensitic BCT phase; in this paper, this

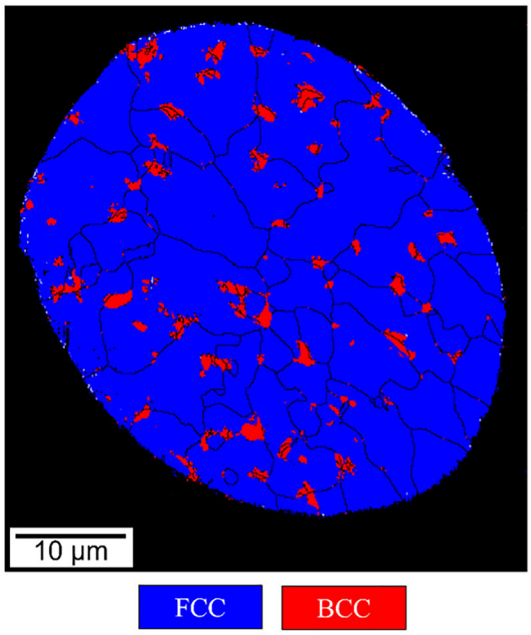

Fig. 1 EBSD of powder used for deposition

phase will be referred to as the BCC phase for simplicity. It should be noted that standard, Hough-based indexing routines in EBSD cannot differentiate between the BCC and BCT phases in steel. The BCC phase in the as-received powder is evenly distributed throughout the powder particle, and the BCC grains are approximately 1-5 μm in size. In the cold spray deposition, the BCC phase also appears to be evenly distributed throughout the deposition and ranges from 1-5 μm in size.

EBSD of the cold spray deposited at a spray gas temperature of 350 °C (Fig. 2a) shows considerably less BCC phase fraction (2.3%) than that deposited at a spray gas temperature of 25 °C (30.5%) (Fig. 2b). The BCC phase fraction in both samples is evenly dispersed over the sample and does not appear to be segregated to any region of the particle after impact. The prior particle interface area in the 25 °C sample provided better indexing than the 350 °C sample.

GSAS-II was used to determine the BCC phase fraction for the as-received powder, the 350 °C cold spray deposition, and the 25 °C cold spray deposit using neutron diffraction (Fig. 3). The 350 °C cold spray deposition shows an average BCC phase fraction of 2.5 % while the as-received powder shows a BCC phase fraction of 2.2%. Reducing the maximum spray gas temperature to 25 °C increased the BCC phase fraction to 30.2%. The 350 °C cold spray deposit reports a slightly higher percentage of BCC than the as-received powder, while the 25 °C deposit reports a significant increase in the BCC phase fraction. This result raises the question of whether this phase fraction increase is evenly distributed over the cold spray

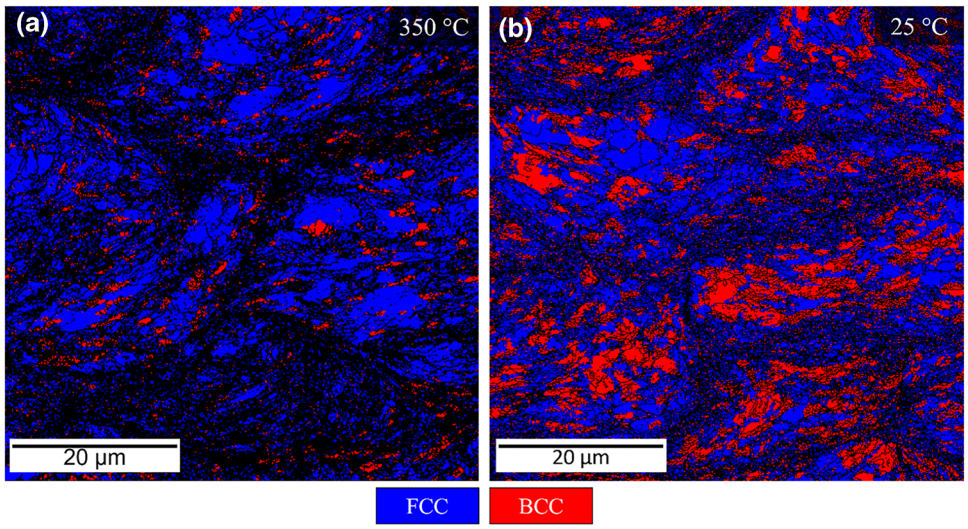

Fig. 2 (a) EBSD phase maps of cold sprayed SS304L using spray gas at 350 °C and (b) spray gas at 25 °C

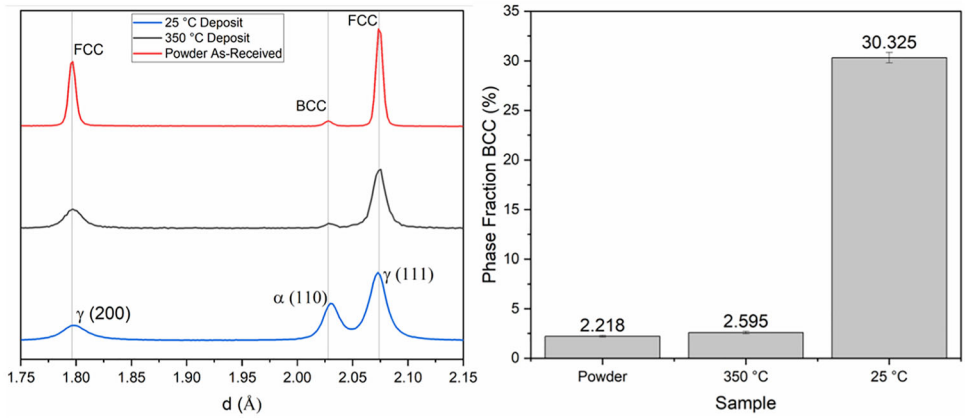

Fig. 3 (a) Neutron diffraction profiles with peaks labeled for as-received powder, 25 °C deposition, and 350 °C deposition. (b) BCC/martensite phase percentage in cold spray deposition as a function of depth with the as-received powder content as a reference

deposit or localized to the prior particle interface. Localization to the prior particle interface could cause issues for corrosion by sensitizing the prior particle interfaces.

TEM bright field images of the prior particle interfaces show a highly deformed microstructure (Fig. 4). TEM of the 350 °C sample shows a band of dynamically recrystallized grains at each prior particle interface, while that at 25 °C shows does not show any clear presence of the equiaxed grains at the prior particle interface. The 25 °C samples show some banded features that are not well described in the literature.

PED maps at the prior particle interfaces show a highly refined microstructure at the prior particle interface with the GOS map indicating dynamically recrystallized grains in this region for the case of the sample sprayed at 350 °C (Fig. 5). Below the prior particle interface, in the material that was impacted from the secondary impact, a refined microstructure with a large grain orientation spread is present in both conditions. For the sample sprayed at room temperature (25 °C) (Fig. 6), a heavily deformed microstructure can be seen with many more elongated, flattened grains than can be seen in the sample sprayed at 350 °C. Additionally, while some nano-size grains can be seen in band contrast maps for the 25 °C sample, there is not a clear band of nanocrystalline grains as seen in the 350 °C sample. The percentage and distribution of the ferrite phase are similar for both samples, with no clear segregation of the phase to any region (Fig. 2). This relative uniformity indicated that the strain-induced martensite phase is not preferentially formed in any specific region in the deposit. For both samples, possible twin boundaries were mapped, indicated by red grain boundaries in the IPF map, with two axis-angle pair definitions for twin boundaries: a recrystallization twin definition of 60° about $< 111 >$ and a deformation twin definition of 60° about $< 112 >$. Neither sample showed a clear presence of twins. Some "twins" were indexed in both samples but aligned with orientation ambiguities from the PED indexing process that is caused by crystallographic symmetry in the diffraction patterns which can result in software having difficulty in distinguishing between two crystallographic

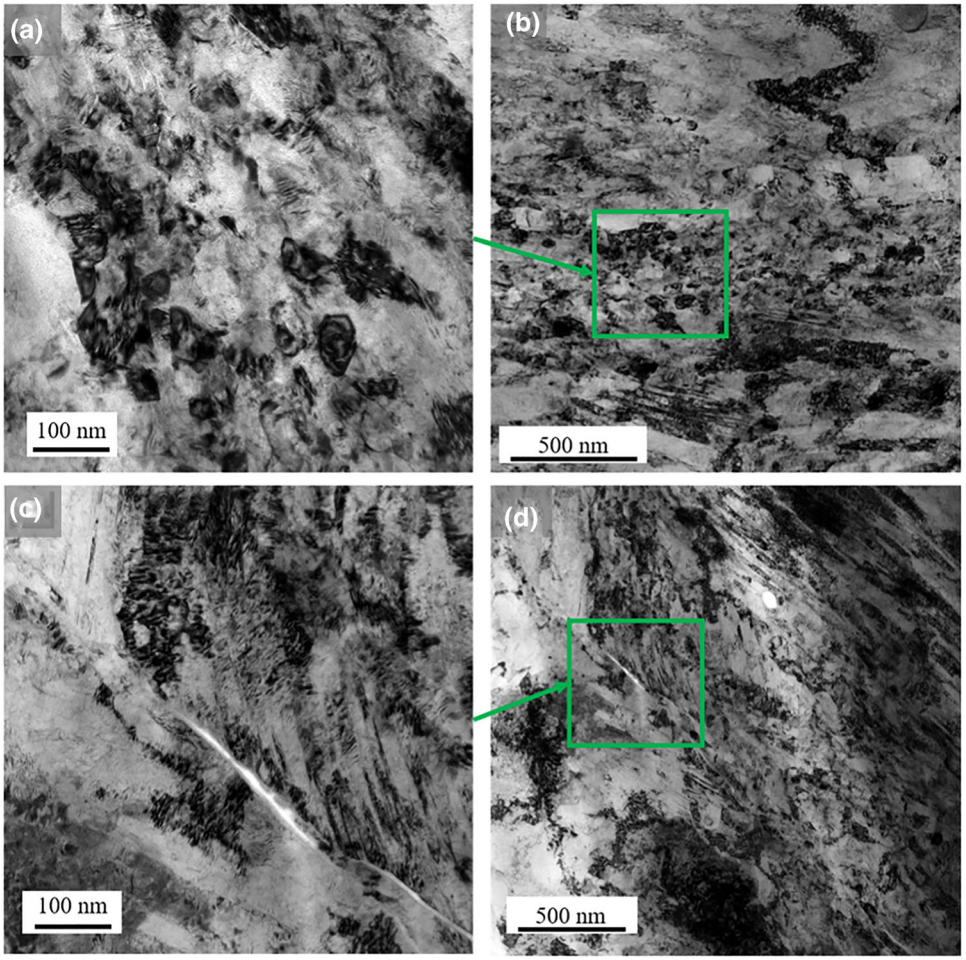

Fig. 4 TEM bright field images of prior particle interfaces showing nanocrystalline grains in the sample sprayed at 350 °C (a, b) and highly deformed grains/banded microstructure with a lack of nanocrystalline equiaxed grains in the sample sprayed at 25 °C (c, d)

symmetric orientations (Ref 35). This is a known issue that can arise from PED.

Discussion

The results in this paper show that cold spray of austenitic stainless steels can form strain-induced martensite and that the extent of this formation is mainly dependent on the spray gas temperature. It is well reported in literature that deformation of austenitic stainless steels, including SS304L, can cause the formation of strain-induced martensite (Ref 6-11), with the phase fraction of martensite reaching as high as 40% in tension and 85% in cold rolled material at room temperature (Ref 6, 21). Additionally, in uniaxial and biaxial tension, both elevated temperatures and high strain rates have been shown to suppress the strain-induced martensite formation, both of which are seen in cold spray (Ref 21, 33). Neutron diffraction of the cold spray deposit shows an increase in 0.4% in the bulk phase fraction of BCC/martensite after deposition at 350 °C and an increase in 28.1% after deposition at room temperature as measured. Examination of the prior particle interface with PED showed a BCC phase at the prior particle interface in both samples, though the formation was much more pronounced in the samples sprayed at 25 °C. Notably, a clear band of equiaxed grains with diminished BCC content is seen just above the prior particle interface in the samples sprayed at 350 °C (Fig. 5), while material sprayed at room temperature shows no evidence of a BCC-free area at the prior particle interface (Fig. 6). Work by Zou et al. showed three distinct regions to exist at the prior particle interface for cold sprayed samples. These three regions provide a valuable framework to discuss the effects seen at the prior particle interface during cold spray deposition as similar results are seen here; these regions are as follows (Fig. 7) (Ref 36):

1. The prior particle interior
2. The transition region between the interface and interior
3. The prior particle interface

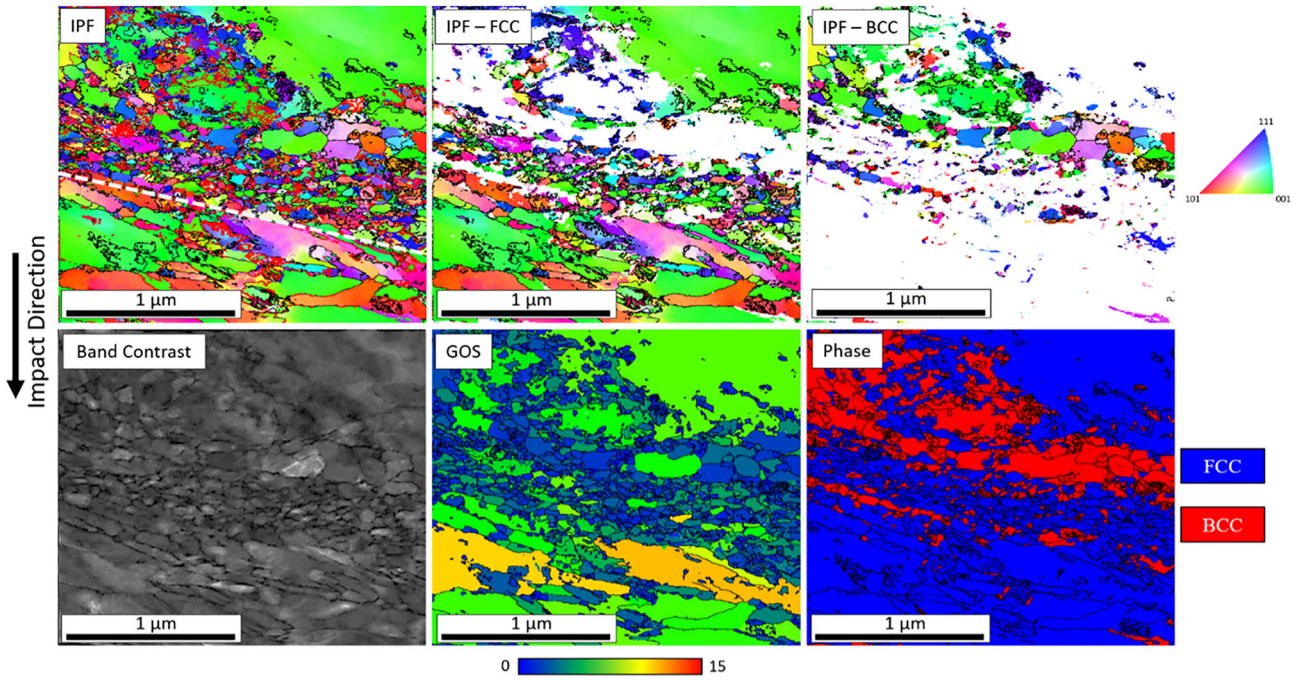

Fig. 5 PED results of 350 °C spray at prior particle interface IPF maps are taken with respect to the impact direction. High-angle grain boundaries (> 15°) are indicated by the black lines. The dotted white line indicates the prior particle interface

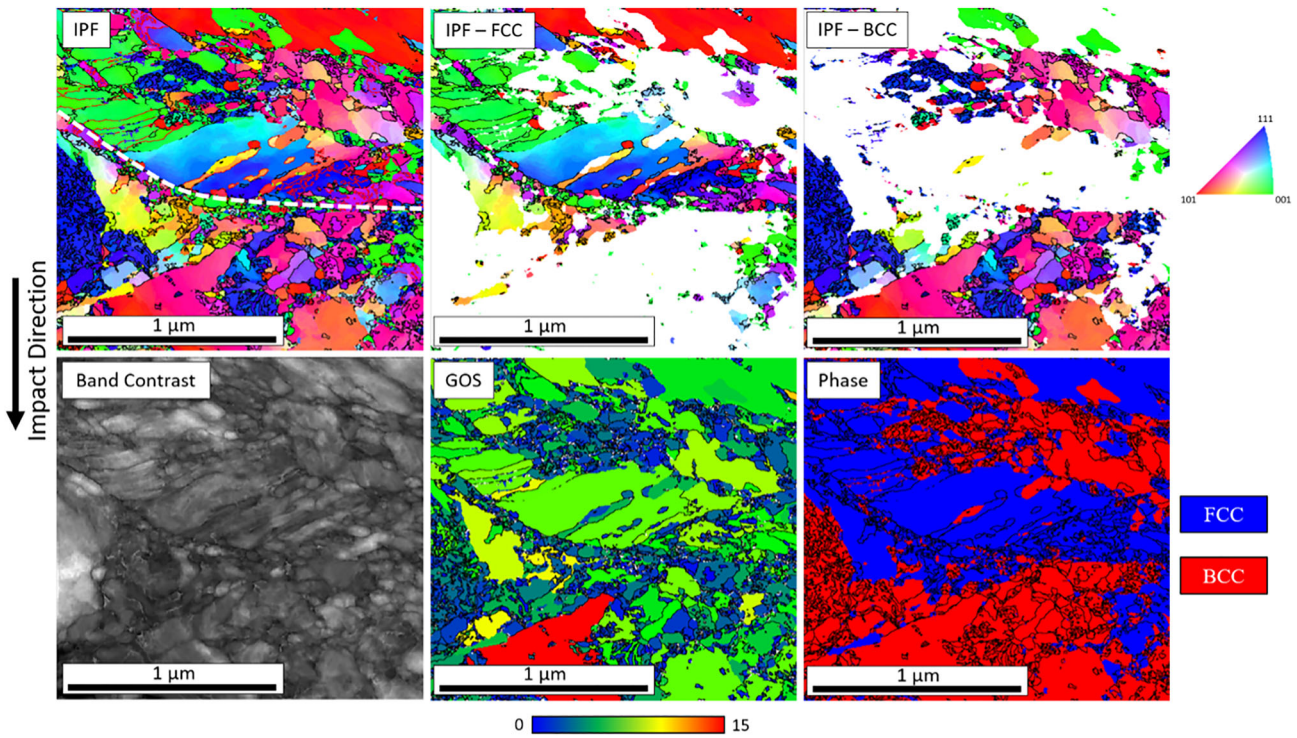

Fig. 6 PED results of 25 °C spray at prior particle interface (dashed white line) IPF maps are taken with respect to the impact direction. High-angle grain boundaries (> 15°) are indicated by the black lines. The dotted white line indicates the prior particle interface

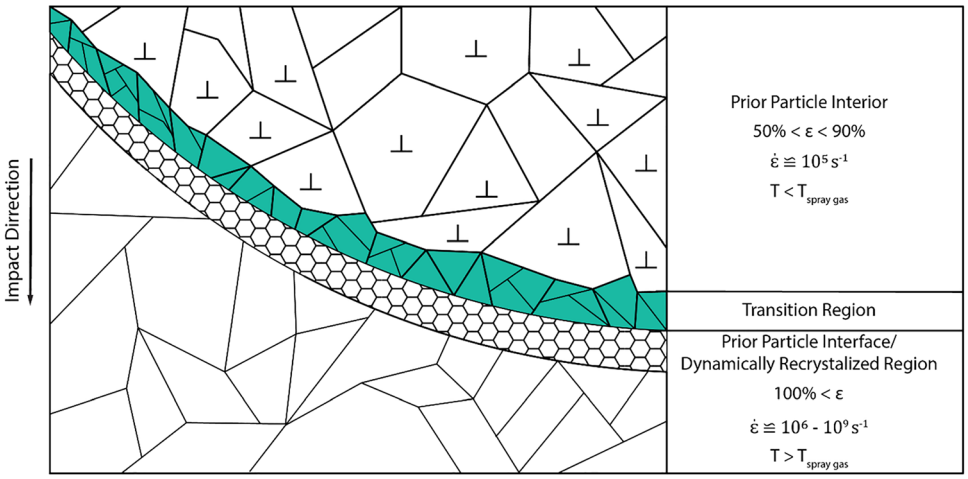

Fig. 7 Schematic representation of an ideal prior particle interface as observed in the present observations of cold spray coatings for the 350 °C spray condition

Table 2 The average measurement of particle dimensions, flattening ratio, and strain for both samples. Given error is the standard deviation for each value of 20 particle impacts

Temperature	w, μm	h, μm	d_0, μm	f_r	ε, %
350 °C	45.3 ± 10.9	18.6 ± 5.45	33.3 ± 7.2	1.36 ± 0.16	60.8 ± 22.7
25 °C	42.5 ± 9.5	19.96 ± 4.7	32.7 ± 5.8	1.29 ± 0.14	50.5 ± 21.2

Conditions in Cold Spray Particles During Impact

It is necessary to understand the strains, strain rates, and temperatures associated with each region in the cold sprayed particle (Fig. 7) to understand the deformation mechanisms seen in each region. For the prior particle interior, the total strain can be reasonably estimated by looking at the shape of the particle after deposition. The total average plastic strain in cold sprayed material can be estimated by measuring the width and height of the particle after impact (Ref 37):

$$f_r = {}^{w}/_{d_0}$$

where w is the width after impact and d_0 is the initial particle diameter. d_0 can be calculated as:

$$d_0 = \sqrt[3]{w^2 h}$$

From this, the average strain ε can be solved as:

$$\varepsilon = \ln\left(\frac{d_0}{h}\right)$$

Twenty grains were measured for each sample to give an average flattening ratio after deposition of 1.36 for the material sprayed at 350 °C and 1.29 for the material sprayed at 25 °C resulting in a total average plastic strain of 60.8% for the 350 °C material and 50.5% for the material sprayed at 25 °C (Table 2).

The average temperature for the prior particle interior can be estimated using numerical simulations of the spray gas speed, temperature, and powder thermal conductivity. The temperature of the powder particles prior to impact can be estimated from simulations to be 120 °C for 15 μm particles and 240 °C for 45 μm particles. These estimates are made using numerical simulations of a 1-D isotropic flow model from K. Sakaki (Ref 38):

$$\frac{dT_p}{dt} = (T_g - T_p)\frac{6h}{c_p \rho_p D_p}$$

where T_p is the particle temperature, h is the heat transfer coefficient, and c_p is the specific heat of the particle, and T_g is calculated as:

$$T_g = T_{gi}\left(\frac{P}{P_i}\right)^{(k-1)/k}$$

where T_g is the gas temperature at any given point along the nozzle's linear direction, T_{gi} is the initial gas temperature at the stagnation point, k is the gas-specific heat ratio, P is the gas pressure, and P_i is the initial gas pressure.

Values such as the strain rates in the material and the temperatures and strains at the prior particle interface are helpful when comparing the microstructures seen in the particle impacts to that seen in literature. While no method exists to measure these values at the current moment, many simulations have been made in literature that can provide

some insight into these values. For example, work by T. Schmidt et al. looked at the temperature distribution in a cold sprayed particle due to adiabatic heating using simulations and estimated temperature increases at the prior particle interface in copper in excess of 750 °C (Ref 39). In addition, in work by Talonen et al. (Ref 40), it was shown that strain rates of only 10^{-1} s^{-1} in tensile testing could cause adiabatic heating, raising the temperature of the material above 80 °C in 301LN stainless steel.

Cold spray literature on the deformation of cold spray particles commonly reports strain rates of 10^{7} s^{-1} to 10^{9} s^{-1} in the adiabatic shear zones (Ref 3-5, 41-49). The strain rate in the prior particle interior is harder to estimate, but some literature suggests that the strain rate in this area is likely 10^{4} to 10^{5} s^{-1} (Ref 3). Based on the literature on the strain-induced martensite transformation at high strain rates, a strain rate of 10^{4} to 10^{5} s^{-1} in the prior particle interior still exceeds the strain rate reported in most literature to impede strain-induced martensite formation significantly. While information on the total strain at the prior particle interface is lacking, it is safe to assume that the strain in this area is well above 100% (Ref 41, 45, 50-53).

Formation of Strain-Induced Martensite in Cold Sprayed SS304L

The extent of the strain-induced martensite transformation in both samples is less than what would be expected at room temperature and quasi-static strain rates. Many authors have shown the formation of strain-induced martensite to have a direct relationship to the total strain experienced during plastic deformation (Ref 20, 21, 25, 32). T. Angel demonstrated this relationship at various formation temperatures, showing approximately 20% strain-induced martensite formation at 50% applied strain and nearly 40% strain-induced martensite at 75 % applied strain (Ref 21). Similarly, work by Shintani et al. showed 70% strain-induced martensite after cold rolling to 50% strain which is considerably more than the 30 % seen in the room-temperature cold spray specimen (Ref 6). From these observations, it is clear that the conditions of cold spray are suppressing the strain-induced martensite transformation.

The temperature of the spray gas is shown to significantly suppress the amount of strain-induced martensite formed during the cold spray deposition process. The deformed material's temperature arguably has the most significant overall effect on suppressing the amount of strain-induced martensite formed. As an example, samples pulled in tension can form as much as 85% martensite when cooled during deformation to − 188 °C , while heating to 80 °C results in as little as 4% martensite (Ref 21). Work by Mukarati et al. simulating the martensite transformation in 301LN stainless steel in tensile deformation showed the volume percentage at various total strains to approach 0% at all temperatures above 120 °C (Ref 54). While little work exists looking at the martensite percentage formed at temperatures much above 100 °C, it can be assumed that limited martensite can be formed at temperatures above 100 °C. Tensile test experiments by Huang et al. (Ref 55) show that at low temperatures (− 80 °C and − 50 °C), martensite formation dominates, and the strain rate sensitivity is proportional to the transformation rate of austenite to martensite. At higher temperatures (25 °C and 135 °C), slip dominates, and the strain rate sensitivity decreases with an increase in strain, an observation that is consistent with most microstructurally stable metal systems. The lack of strain-induced martensite in the samples sprayed at elevated temperatures is consistent with the literature. Many authors show that increasing the temperature of the material being deformed will limit the strain-induced martensite transformation considerably at all strain rates. The heating of the particles as they travel through the cold spray system and the adiabatic heating caused by deformation likely causes a temperature rise to the point where strain-induced martensite is not formed in the prior particle interior after cold spray. These findings are also consistent with the present literature on the cold spray of austenitic stainless steels, as all current literature uses spray temperatures above 100 °C.

The cold spray sample sprayed at 25 °C shows lower amounts of strain-induced martensite (30.325%) when compared to that expected at quasi-static strain rates at 25 °C (>80%), which can be expected by the higher strain rate in cold spray (Ref 54). Literature shows that the strain rate can play a significant role in suppressing the strain-induced martensite phase transformation. Research shows that high strain rates can inhibit strain-induced martensite formation, pointing to both adiabatic heating due to plastic deformation and twinning being responsible for a deviation from the expected strain-induced martensite formation (Ref 32-34, 56). These strain rates are not easily achievable in other metal deformation techniques, with the highest strain rates reported in literature being approximately 10^{5} s^{-1}. Work by Chen et al. using surface mechanical attrition treatment (SMAT) show that at high strain rates (10^{5} s^{-1}) the formation of strain-induced martensite is impeded due to a change in deformation mechanism from glide-based plasticity to deformation twinning, resulting in the formation of ultra-fine grains and dislocation pileup as observed in the TEM (Ref 56). Chen et al.'s work indicate that when strain rates are low, dislocation-based activities such as accumulation, interaction, tangling, and spatial rearrangement, as well as the austenite to martensite transformation, are the primary deformation

mechanisms. However, at higher strain rates, deformation twinning becomes the dominant mechanism. In the present work, no clear indication of twins was observed in either cold sprayed deposit. Additionally, it is worth noting that the twins seen in the work by Chen et al. are much finer than any of the features seen in TEM or PED in either of the samples in this paper. Furthermore, shock loading experiments such as the work by Staudhammer et al. may approach the strain rates seen in cold spray as these experiments have a strain rate which is difficult to estimate but are likely in excess of 10^4 s^{-1}. These shock loading experiments show approximately 1% to 4% martensite formed depending on temperature and shock pressure, with the stress state and temperature rise during shock loading suppressing the strain-induced martensite. Additionally, work by Staudhammer et al. showed that the α' phase in shock loading experiments formed at shear bands only.

Many authors attribute the lack of strain-induced martensite at high strain rates to be predominantly due to adiabatic heating in the high strain rate regions. Work by Sunil et al. looked at the formation of strain-induced martensite in high strain rate compression tests using a split-Hopkinson bar setup (Ref 57). The work by Sunil et al. also examined the effect of strain rate in compression on strain-induced martensite in which a 1-D heat transfer equation was used to determine the maximum temperature due to adiabatic heating. The maximum temperature was estimated to be 120 °C, and it was shown that this elevated temperature impeded the strain-induced martensite transformation for SS304L. Furthermore, this work by Sunil et al. found that the formation of strain-induced martensite decreased with strain rate for all strains above 0.15. At a strain rate of 10^3 s^{-1} and strain of 50% slightly less than 20%, strain-induced martensite was formed. This amount is considerably less than the 30% seen here for cold spray at room temperature. This comparison means more strain-induced martensite is formed in the cold spray at the calculated average strain and expected strain rate of cold spray than in non-cold spray literature. The amount of strain-induced martensite measured in the cold spray produced at room temperature is equal to that observed in the work by Sunil et al. at a strain rate of 1 s^{-1} and a strain of 0.8. This difference could be due to the peening effects seen by the cold spray material by the subsequent impact of powder particles, or it could be due to the more complex strain field seen in a particle impact that will not be entirely compressive in nature. In work by Chen et al., the SMAT process, which creates a peening force, produced approximately 22% strain-induced martensite near the peened surface, which had a strain rate of 9×10^4 s^{-1}, which is in reasonable agreement with the amount of strain-induced martensite that we report here for the room temperature, cold sprayed sample. It should be noted that the likely cause of the BCC/BCT phases in the as-received powder is the high cooling rate seen by the powder during inert gas atomization since martensite is a metastable phase that can form when liquid steel cools rapidly from a molten state so that the stable austenitic room temperature phases cannot form (Ref 58). This is distinctly different from the formation of strain-induced martensite, and it is not clear if some fraction of this initial martensite phase in the powder is retained in the deposits or if elevated spray temperatures would work to reduce this phase or only limit the formation of new strain-induced martensite.

The conclusions of the present study are consistent with the results seen previously in literature for cold spray of 304L. Based on the above discussion, it can be expected that strain-induced martensite will be formed preferentially at lower temperatures, whereas the transformation will be inhibited by higher temperatures and strain rates. In literature, it is seen that deposits made from powder with no initial BCC phase fraction typically showed no BCC phase fraction when measured via XRD or EBSD, those with BCC in the powder showed a BCC phase fraction in the deposit, and some findings suggest cold spray performed at higher spray gas temperatures resulted in the reduction of the BCC phase fraction in the cold sprayed material when compared to the powder feedstock.

Effect of Spray Temperature on the Microstructure at the Prior Particle Interfaces

It is worth noting that in the samples produced at 25 °C, a band of dynamically recrystallized grains is not clearly seen as it is in the sample produced at 350 °C (Fig. 5-6). For cold sprayed materials, the presence of ultrafine grains at prior particle interfaces has been reported in literature many times and is believed to be caused by the ultra-high strain rate deformation at the prior particle interfaces (Ref 2, 4, 36, 42, 43, 59). It is usually described in literature that these grains are the result of "dynamic recrystallization", though many mechanisms have been proposed that could cause this effect. These mechanisms are outlined in work by Rokni et al. and Liu et al. and include continuous dynamic recrystallization (CDRX), geometric dynamic recrystallization (GDRX), rotational dynamic recrystallization (RDRX), progressive subgrain misorientation recrystallization (PriSM), static recovery (SRV), and static recrystallization (SRX) (Ref 2, 60). The GDRX and RDRX are all forms of the broader CDRX umbrella, which include the continuous recrystallization of grains during deformation through the means of diffusion. SRV and SRX are forms of recrystallization that are proposed to form due to residual heat and peening stresses due to subsequent impacts, which also require diffusion. The PriSM mechanism models mechanically driven lattice rotations within

an adiabatic shear band that result in recrystallization, which unlike the other proposed mechanisms, does not rely on diffusion, which is argued to be too slow for recrystallization in high strain rates such as that seen in cold spray. This paper's data is insufficient to definitively support any of the proposed dynamic recrystallization models for cold spray. However, the following is intended to add to the discussion currently in literature and highlight how the observed microstructure and the effect of temperature on the microstructure at the prior particle interface can be interpreted in light of each proposed mechanism.

While SRX and SRV have both been shown in CS materials, the low stacking fault energy of SS304L would support SRX. SRX is more likely than SRV in low stacking fault energy materials because recovery is limited due to dissociated dislocations resulting in nucleation and recrystallization to be more likely (Ref 61). Additionally, literature has shown the presence of CDRX in cold rolled SS304L. While SS304L typically prefers discontinuous dynamic recrystallization (DDRX) due to its low stacking fault energy, literature has shown that decreasing the grain size in 304L from 35 to 8 μm can shift the recrystallization mechanism to CDRX. The average grain size in the as-atomized powders is less than 10 μm which would support the formation of CDRX (Ref 62). Additionally, it has been shown that the formation of CDRX can occur in type 304 stainless steel at elevated temperatures of 800 to 1000 °C during cold rolling of heat treated material with an initial grain size of 7 μm and could result in grain sizes as small as 1 μm (Ref 63). It is worth noting that DDRX has been shown in simulations of type 304 stainless steel for an initial grain size of 35 μm at 1000 °C, where at a strain of 3.0, 100% recrystallization had occurred, resulting in a predicted grain size of 6 microns. This predicted grain size is an order of magnitude larger than the measured grain size seen in TEM of cold sprayed material (Ref 64).

Dynamic recrystallization through diffusion-based means has been previously described in cold sprayed materials, with the most reported mechanism for recrystallization being a diffusion-based rotational dynamic recrystallization mechanism. The diffusion-based rotational dynamic recrystallization mechanism was first described by Meyers et al. for high strain rate deformation of 304 stainless steel using a Hopkinson bar where the argument is made that at high strain rates (10^4 s^{-1}) diffusion at the grain boundaries, which is much faster than bulk diffusion, allows for grain boundary reorientation and dynamically recrystallized grains (Ref 65). This same method was proposed for dynamic recrystallization in cold spray in work by Zou et al. for cold sprayed nickel (Ref 36). Dynamic recrystallization, as described by Zou et al., begins with the formation of elongated subgrains at the prior particle interfaces due to the high dislocation density formed during cold spray; these subgrains continue to evolve and form further subgrains due to additional dislocation formation as the strain at the particle interface increases. At this point, small, refined subgrains exist at the prior particle interface separated by low-angle grain boundaries. As more strain occurs, the misorientations between these subgrains increase to accommodate this deformation by rotating. This rotation forms small, dynamically formed recrystallized grains separated by high-angle grain boundaries (Ref 66). The approximate grain size caused by dynamics recrystallization via this method can be approximated using the relationship (Ref 67):

$$\left(\frac{\sigma}{G}\right)\left(\frac{D_r}{b}\right)^n = k$$

where n and K are constants (0.8 and 15, respectively), b is the burger vector, D_r is the dynamically recrystallized grain size, G is the shear modulus, and σ is the applied stress. For cold spray, σ can be described by the mean pressure during impact approximated as $\sigma = 0.5\rho v^2$ where ρ is the density of the material and v is the velocity. This material gives a grain size of 50-125 nm, which is within the range measured in the present PED results.

The PriSM mechanism for dynamic recrystallization provides an intriguing theory of dynamic recrystallization in high-strain rate materials (Ref 68). The PriSM mechanism asserts that other models do not sufficiently describe the observed dynamic recrystallization grain size in high strain rate materials and proposes that mechanical rotation of subgrains during deformation and boundary refinement via diffusion during cooling occur at shear bands to explain much smaller grain sizes. This mechanism is consistent with the findings of fine, dynamically recrystallized grains on the order of 100 nm (0.1 μm) in this paper. Work by Rojas et al. provides more evidence for rotation-based dynamic recrystallization in cold spray materials being possible without the need for diffusion (Ref 69). In Rojas's work, both experiments and simulations show the formation of dynamically recrystallized grains in silver nanocube high-velocity impacts. The paper proposed that the large shock wave stress and high dislocation density in the nanocubes were not sufficient for recrystallization alone. Instead, the pathway for recrystallization was hypothesized to be that the shock loads during impact produced a considerable amount of boundaries, such as grain boundaries and twins, and that once these are developed, the lattice rotates within these boundaries through the large shear stresses caused by the shock wave. This mechanism occurs without the need for diffusion and accounts for the gradient in properties seen in cold spray particle impacts due to the decreasing shockwave pressure away from the impact

surface. The exact mechanism for dynamic recrystallization in cold spray is still unclear and needs further investigation, though the lack of ultrafine grains in lower-temperature sprays provides some additional context to the proposed mechanisms.

Conclusions

In conclusion, it has been shown that cold spray deposition can produce strain-induced martensite and that the extent of this transformation is mainly dependent on the spray gas temperature. Additionally, the reduction of the spray gas temperature was seen to influence the microstructure at the prior particle interface region. While EBSD results cannot definitively show the phase fraction of martensite in cold spray due to the limited sample area and difficulty in indexing the prior particle interface regions, neutron diffraction data clearly shows a slight increase in the BCC/BCT phase from the as-received powder in cold spray material produced at a spray gas temperature of 350 °C and a much more significant increase of 30% in that produced using a spray gas temperature of 25 °C. The literature gives compelling evidence to believe that the thermomechanical conditions that exist in cold spray at elevated temperatures significantly reduce the amount of strain-induced martensite formed. If spray temperatures can be increased further without clogging the cold spray nozzles, cold spray could reduce the formation of strain-induced martensite *in situ* without needing post-heat treatments on the material. A summary of the findings is given below:

- Neutron diffraction showed a 0.4% increase in BCC phase/martensite after cold spray of the powder particles at 350 °C and an increase in 28.1% when sprayed at 25 °C showing that the strain-induced martensite transformation can occur in cold spray and that a correlation between spray temperature and the strain induced martensite transformation exists.
- These findings suggest that adiabatic heating due to the high strain rates, large total strains, and the heat input from the spray gas work together to suppress the strain-induced martensite transformation throughout the cold spray deposit.
- A more substantial presence of ultrafine grains, possibly due to dynamic recrystallization, was seen at the prior particle interface in the samples sprayed at 350 °C as compared to those sprayed at 25 °C, indicating that the spray temperature plays a role in the ability for these recrystallized grains to form at the prior particle interfaces.
- This work suggests that the strain-induced martensite transformation can be suppressed or eliminated with sufficiently high spray gas temperature if nozzle fouling can be controlled at elevated temperatures.

Acknowledgments This research was supported by NEUP 18-15372 Work scope FC-4.2; Contract DE-NE0008770. Neutron diffraction was performed by the VULCAN beamline at the SNS facility at ORNL.

Competing interest The authors declare that they have no known competing financial interests or personal relationships that could have appeared to influence the work reported in this paper.

References

1. J. Villafuerte, *Modern Cold Spray: Materials, Process, and Applications*, Springer, New York, 2015.
2. T. Liu, J.D. Leazer, and L.N. Brewer, Particle Deformation and Microstructure Evolution During Cold Spray of Individual Al-Cu Alloy Powder Particles, *Acta Mater.*, 2019, **168**, p 13-23.
3. V. Lemiale, P. King, M. Rudman, M. Prakash, P. Cleary, M. Jahedi, and S. Gulizia, Temperature and Strain Rate Effects in Cold Spray Investigated by Smoothed Particle Hydrodynamics, *Surf. Coat. Technol.*, 2014, **254**, p 121-130.
4. P.C. King, S.H. Zahiri, and M. Jahedi, Microstructural Refinement Within a Cold-Sprayed Copper Particle, *Metall. Mater. Trans. A*, 2009, **40**(9), p 2115-2123.
5. K. Spencer and M.X. Zhang, Optimisation of Stainless Steel Cold Spray Coatings Using Mixed Particle Size Distributions, *Surf. Coat. Technol.*, 2011, **205**(21-22), p 5135-5140.
6. T. Shintani and Y. Murata, Evaluation of the Dislocation Density and Dislocation Character in Cold Rolled Type 304 Steel Determined by Profile Analysis of X-ray Diffraction, *Acta Mater.*, 2011, **59**(11), p 4314-4322.
7. J.-Y. Choi and W. Jin, Strain Induced Martensite Formation and Its Effect on Strain Hardening Behavior in the Cold Drawn 304 Austenitic Stainless Steels, *Scr. Mater.*, 1997, **36**(1), p 99-104.
8. I. Tamura, Deformation-Induced Martensitic Transformation and Transformation-Induced Plasticity in Steels, *Metal Sci.*, 1982, **16**(5), p 245-253.
9. J. Post, H. Nolles, K. Datta, and H.J. Geijselaers, Experimental Determination of the Constitutive Behaviour of a Metastable Austenitic Stainless Steel, *Mater. Sci. Eng. A*, 2008, **498**(1-2), p 179-190.
10. M. Radu, J. Valy, A.-F. Gourgues, F. Le Strat, and A. Pineau, Continuous Magnetic Method for Quantitative Monitoring of Martensitic Transformation in Steels Containing Metastable Austenite, *Scr. Mater.*, 2005, **52**(6), p 525-530.
11. J.A. Lichtenfeld, C.J. Van Tyne, and M.C. Mataya, Effect of Strain Rate on Stress-Strain Behavior of Alloy 309 and 304L Austenitic Stainless Steel, *Metall. Mater. Trans. A*, 2006, **37**(1), p 147-161.
12. A.-M. Bandar, P. Vo, R. Mongrain, E. Irissou, and S. Yue, Effect of Heat Treatment on the Microstructure and Mechanical Properties of Stainless Steel 316L Coatings Produced by Cold Spray for Biomedical Applications, *J. Therm. Spray Technol.*, 2014, **23**(4), p 641-652.
13. C.M. Roper, A. Heczel, V.S. Bhattiprolu, T. Kolonits, J. Gubicza, and L.N. Brewer, Effect of Laser Heating on Microstructure and Deposition Properties of Cold Sprayed SS304L, *Materialia*, 2022, **22**, p 101372.
14. J. Frattolin, R. Roy, S. Rajagopalan, M. Walsh, S. Yue, O.F. Bertrand, and R. Mongrain, A Manufacturing and Annealing Protocol to Develop a Cold-Sprayed Fe-316L Stainless Steel

Biodegradable Stenting Material, *Acta Biomater.*, 2019, **99**, p 479-494.
15. H. Yeom, T. Dabney, N. Pocquette, K. Ross, F.E. Pfefferkorn, and K. Sridharan, Cold Spray Deposition of 304L Stainless Steel to Mitigate Chloride-Induced Stress Corrosion Cracking in Canisters for Used Nuclear Fuel Storage, *J. Nucl. Mater.*, 2020, **538**, p 152254.
16. L. Brewer, J. Schiel, E. Menon, and D. Woo, The Connections Between Powder Variability and Coating Microstructures for Cold Spray Deposition of Austenitic Stainless Steel, *Surf. Coat. Technol.*, 2018, **334**, p 50-60.
17. M. Villa, S. Dosta, and J.M. Guilemany, Optimization of 316L Stainless Steel Coatings on Light Alloys Using Cold Gas Spray, *Surf. Coat. Technol.*, 2013, **235**, p 220-225.
18. B. Dikici, H. Yilmazer, I. Ozdemir, and M. Isik, The Effect of Post-Heat Treatment on Microstructure of 316L Cold-Sprayed Coatings and Their Corrosion Performance, *J. Therm. Spray Technol.*, 2016, **25**(4), p 704-714.
19. C. Borchers, T. Schmidt, F. Gärtner, and H. Kreye, High Strain Rate Deformation Microstructures of Stainless Steel 316L by Cold Spraying and Explosive Powder Compaction, *Appl. Phys. A*, 2007, **90**(3), p 517-526.
20. E. Scheil, Über die Umwandlung des Austenits in Martensit in Eisen-Nickellegierungen unter Belastung, *Z. Anorg. Allg. Chem.*, 1932, **207**(1), p 21-40.
21. T. Angel, Formation of Martensite in Austenitic Stainless Steels Effects of Deformation, Temperature, and Composition, *J. Iron Steel Inst.*, 1954, **177**, p 165-174.
22. J. Venables, The Martensite Transformation in Stainless Steel, *Philos. Mag. A J. Theor. Exp. Appl. Phys.*, 1962, **7**(73), p 35-44.
23. R. Lagneborgj, The Martensite Transformation in 18% Cr-8% Ni Steels, *Acta Metall.*, 1964, **12**(7), p 823-843.
24. P.L. Mangonon and G. Thomas, The Martensite Phases in 304 Stainless Steel, *Metall. Trans.*, 1970, **1**(6), p 1577-1586.
25. D. Goodchild, W. Roberts, and D. Wilson, Plastic Deformation and Phase Transformation in Textured Austenitic Stainless Steel, *Acta Metall.*, 1970, **18**(11), p 1137-1145.
26. G. Olson and M. Cohen, A Mechanism for the Strain-Induced Nucleation of Martensitic Transformations, *J. Less Common Metals*, 1972, **28**(1), p 107-118.
27. G. Olson and M. Cohen, Kinetics of Strain-Induced Martensitic Nucleation, *Metall. Trans. A*, 1975, **6**(4), p 791-795.
28. G.B. Olson and M. Cohen, A general mechanism of martensitic nucleation: Part I General concepts and the FCC→ HCP transformation, *Metall. Trans. A*, 1976, **7**(12), p 1897-1904.
29. G. Olson and M. Cohen, A General Mechanism of Martensitic Nucleation: Part II. FCC→ BCC and Other Martensitic Transformations, *Metall. Trans. A*, 1976, **7**(12), p 1905-1914.
30. G. Olson and M. Cohen, A General Mechanism of Martensitic Nucleation: Part III. Kinetics of Martensitic Nucleation, *Metall. Trans. A*, 1976, **7**(12), p 1915-1923.
31. L. Murr and K. Staudhammer, Effect of Stress Amplitude and Stress Duration on Twinning and Phase Transformations in Shock-Loaded and Cold-Rolled 304 Stainless Steel, *Mater. Sci. Eng.*, 1975, **20**, p 35-46.
32. S. Hecker, M. Stout, K. Staudhammer, and J. Smith, Effects of Strain State and Strain Rate on Deformation-Induced Transformation in 304 Stainless Steel: Part I. Magnetic Measurements and Mechanical Behavior, *Metall. Trans. A*, 1982, **13**(4), p 619-626.
33. L. Murr, K. Staudhammer, and S. Hecker, Effects of Strain State and Strain Rate on Deformation-Induced Transformation in 304 Stainless Steel: Part II. Microstructural Study, *Metall. Trans. A*, 1982, **13**(4), p 627-635.
34. K. Staudhammer, C. Frantz, S. Hecker, L. Murr, Effects of strain rate on deformation-induced martensite in 304 stainless steel, Shock Waves and high-strain-rate phenomena in metals, Springer 1981, pp. 91-112.
35. J. Brons and G. Thompson, Orientation Mapping via Precession-Enhanced Electron Diffraction and Its Applications in Materials Science, *JOM*, 2014, **66**, p 165-170.
36. Y. Zou, W. Qin, E. Irissou, J.-G. Legoux, S. Yue and J.A. Szpunar, Dynamic Recrystallization in the Particle/Particle Interfacial Region of Cold-Sprayed Nickel Coating: Electron Backscatter Diffraction Characterization, *Scr. Mater.*, 2009, **61**(9), p 899-902.
37. V.K. Champagne, D.J. Helfritch, M.D. Trexler, and B.M. Gabriel, The effect of Cold Spray Impact Velocity on Deposit Hardness, *Modell. Simul. Mater. Sci. Eng.*, 2010, **18**(6), p 065011.
38. K. Sakaki, The influence of nozzle design in the cold spray process, The cold spray materials deposition process, Elsevier2007, pp. 117-126.
39. T. Schmidt, H. Assadi, F. Gärtner, H. Richter, T. Stoltenhoff, H. Kreye, and T. Klassen, From Particle Acceleration to Impact and Bonding in Cold Spraying, *J. Therm. Spray Technol.*, 2009, **18**(5), p 794-808.
40. J. Talonen, H. Hänninen, P. Nenonen, and G. Pape, Effect of Strain Rate on the Strain-Induced $\gamma \rightarrow \alpha'$-Martensite Transformation and Mechanical Properties of Austenitic Stainless Steels, *Metall. Mater. Trans. A*, 2005, **36**(2), p 421-432.
41. H. Assadi, F. Gärtner, T. Stoltenhoff, and H. Kreye, Bonding Mechanism in Cold Gas Spraying, *Acta Mater.*, 2003, **51**(15), p 4379-4394.
42. Y. Zou, D. Goldbaum, J.A. Szpunar, and S. Yue, Microstructure and Nanohardness of Cold-Sprayed Coatings: Electron Backscattered Diffraction and Nanoindentation Studies, *Scr. Mater.*, 2010, **62**(6), p 395-398.
43. M. Rokni, C. Widener, and V. Champagne, Microstructural Evolution of 6061 Aluminum Gas-Atomized Powder and High-Pressure Cold-Sprayed Deposition, *J. Therm. Spray Technol.*, 2014, **23**(3), p 514-524.
44. L. Ajdelsztajn, A. Zuniga, B. Jodoin, and E. Lavernia, Cold gas Dynamic Spraying of a High Temperature Al Alloy, *Surf. Coat. Technol.*, 2006, **201**(6), p 2109-2116.
45. T. Schmidt, F. Gärtner, H. Assadi, and H. Kreye, Development of a Generalized Parameter Window for Cold Spray Deposition, *Acta Mater.*, 2006, **54**(3), p 729-742.
46. K. Kang, J. Won, G. Bae, S. Ha, and C. Lee, Interfacial Bonding and Microstructural Evolution of Al in Kinetic Spraying, *J. Mater. Sci.*, 2012, **47**(11), p 4649-4659.
47. K. Kim, M. Watanabe, and S. Kuroda, Bonding Mechanisms of Thermally Softened Metallic Powder Particles and Substrates Impacted at High Velocity, *Surf. Coat. Technol.*, 2010, **204**(14), p 2175-2180.
48. P.C. King, G. Bae, S.H. Zahiri, M. Jahedi, and C. Lee, An experimental and Finite Element Study of Cold Spray Copper Impact onto Two Aluminum Substrates, *J. Therm. Spray Technol.*, 2010, **19**(3), p 620-634.
49. Y. Xiong, K. Kang, G. Bae, S. Yoon, and C. Lee, Dynamic Amorphization and Recrystallization of Metals in Kinetic Spray Process, *Appl. Phys. Lett.*, 2008, **92**(19), p 194101.
50. K. Loke, Z.-Q. Zhang, S. Narayanaswamy, P.K. Koh, V. Luzin, T. Gnaupel-Herold, and A.S.M. Ang, Residual Stress Analysis of Cold Spray Coatings Sprayed at Angles Using Through-Thickness Neutron Diffraction Measurement, *J. Therm. Spray Technol.*, 2021, **30**, p 1-17.
51. S. Msolli, Z.-Q. Zhang, D.H.L. Seng, Z. Zhang, J. Guo, C. Reddy, N. Sridhar, J. Pan, B.H. Tan, and Q. Loi, An Experimentally Validated Dislocation Density Based Computational Framework for Predicting Microstructural Evolution in Cold Spray Process, *Int. J. Solids Struct.*, 2021, **225**, p 111065.

52. M. Hassani-Gangaraj, D. Veysset, V.K. Champagne, K.A. Nelson, and C.A. Schuh, Adiabatic Shear Instability is Not Necessary for Adhesion in Cold Spray, *Acta Mater.*, 2018, **158**, p 430-439.
53. C. Borchers, F. Gärtner, T. Stoltenhoff, and H. Kreye, Formation of Persistent Dislocation Loops by Ultra-High Strain-Rate Deformation During Cold Spraying, *Acta Mater.*, 2005, **53**(10), p 2991-3000.
54. T.W. Mukarati, R.J. Mostert, and C.W. Siyasiya, Modeling of the Kinetics of Strain-Induced Martensite Transformation and the Transformation-Induced Plasticity Effect in a Lean-Alloyed Metastable Austenitic Stainless Steel, *Steel Res. Int.*, 2022, **93**(5), p 2100459.
55. G. Huang, D. Matlock, and G. Krauss, Martensite Formation, Strain Rate Sensitivity, and Deformation Behavior of Type 304 Stainless Steel Sheet, *Metall. Trans. A*, 1989, **20**(7), p 1239-1246.
56. A. Chen, H. Ruan, J. Wang, H. Chan, Q. Wang, Q. Li, and J. Lu, The Influence of Strain Rate on the Microstructure Transition of 304 Stainless Steel, *Acta Mater.*, 2011, **59**(9), p 3697-3709.
57. S. Sunil and R. Kapoor, Effect of Strain Rate on the Formation of Strain-Induced Martensite in AISI 304L Stainless Steel, *Metall. Mater. Trans. A*, 2020, **51**(11), p 5667-5676.
58. R.N. Wright, J.E. Flinn, G.E. Korth, J.C. Bae, and T.F. Kelly, The Microstructure and Phase Relationships in Rapidly Solidified Type 304 Stainless Steel Powders, *Metall. Trans. A*, 1988, **19**(10), p 2399-2405.
59. C. Borchers, F. Gärtner, T. Stoltenhoff, and H. Kreye, Microstructural Bonding Features of Cold Sprayed Face Centered Cubic Metals, *J. Appl. Phys.*, 2004, **96**(8), p 4288-4292.
60. M. Rokni, S. Nutt, C. Widener, V. Champagne, and R. Hrabe, Review of Relationship Between Particle Deformation, Coating Microstructure, and Properties in High-Pressure Cold Spray, *J. Therm. Spray Technol.*, 2017, **26**(6), p 1308-1355.
61. A.T. Krawczynska, M. Kerber, P. Suchecki, B. Romelczyk-Baishya, M. Lewandowska, and D. Setman, The Impact of the Stacking Fault Energy of Nanostructured Metals on Phenomena During Annealing at the High Hydrostatic Pressure, *Mater. Sci. Eng. A*, 2021, **808**, p 140913.
62. A. Dehghan-Manshadi and P. Hodgson, Dependency of Recrystallization Mechanism to the Initial Grain Size, *Metall. Mater. Trans. A*, 2008, **39**(12), p 2830-2840.
63. Z. Yanushkevich, A. Belyakov, and R. Kaibyshev, Microstructural Evolution of a 304-Type Austenitic Stainless Steel During Rolling at Temperatures of 773–1273 K, *Acta Mater.*, 2015, **82**, p 244-254.
64. P. Bernard, S. Bag, K. Huang, and R.E. Logé, A Two-Site Mean Field Model of Discontinuous Dynamic Recrystallization, *Mater. Sci. Eng. A*, 2011, **528**(24), p 7357-7367.
65. M. Meyers, Y. Xu, Q. Xue, M. Perez-Prado, and T. McNelley, Microstructural Evolution in Adiabatic Shear Localization in Stainless Steel, *Acta Mater.*, 2003, **51**(5), p 1307-1325.
66. X.-T. Luo, C.-X. Li, F.-L. Shang, G.-J. Yang, Y.-Y. Wang, and C.-J. Li, High Velocity Impact Induced Microstructure evolution During Deposition of Cold Spray Coatings: A Review, *Surf. Coat. Technol.*, 2014, **254**, p 11-20.
67. F.J. Humphreys and M. Hatherly, *Recrystallization and Related Annealing Phenomena*, Elsevier, New York, 2012.
68. J.A. Hines, K.S. Vecchio, and S. Ahzi, A Model for Microstructure Evolution in Adiabatic Shear Bands, *Metall. Mater. Trans. A*, 1998, **29**(1), p 191-203.
69. D.F. Rojas, O.K. Orhan, and M. Ponga, Dynamic Recrystallization of Silver Nanocubes During High-Velocity Impacts, *Acta Mater.*, 2021, **212**, p 116892.